

A self-consistent model of isolated neutron stars: the case of the X-ray pulsar RX J0720.4-3125

J.F. Pérez-Azorín¹, J.A. Pons¹, J.A. Miralles¹, and G. Miniutti²

¹ Departament de Física Aplicada, Universitat d'Alacant, Ap. Correus 99, 03080 Alacant, Spain

² Institute of Astronomy, University of Cambridge, Madingley Road, Cambridge, CB3 0HA, UK

Received...../ Accepted.....

Abstract. We present a unified explanation for the observed properties of the isolated neutron star RX J0720.4-3125 by obtaining a self-consistent model that accounts simultaneously for the observed X-ray spectrum and optical excess, the pulsed fraction, the observed spectral feature around 0.3 keV, and the long-term spectral evolution. We show that all observed properties are consistent with a normal neutron star with a proper radius of about 12 km, a temperature at the magnetic pole of about 100 eV and a magnetic field strength of 2×10^{13} G, value inferred from the observed period decay. The high magnetic field produces a strong anisotropy in the surface temperature distribution. The observed variability of the effective temperature, strength of the spectral feature, and pulsed fraction are in good agreement with the predictions of our model in which the star is subject to free precession, producing changes in the angle between the magnetic field and the rotation axis of tens of degrees with a periodicity of 7 years, as pointed out by other authors on the basis of phenomenological models. In addition to the evidence of internal toroidal components, we also find strong evidence of non-dipolar magnetic fields, since all spectral properties are better reproduced with models with strong quadrupolar components.

Key words. Stars: neutron - Stars: magnetic fields - Stars: individual: RX J 0720.4-3125 - Radiation mechanisms: thermal - X-rays: stars

1. Introduction

RX J0720.4-3125 belongs to the family of radio-quiet isolated neutron stars (INS), a puzzling group of compact objects that during the last decade have provoked speculations about their real nature (neutron stars or strange stars) and forced us to reconsider the thermal emission mechanisms. RX J0720.4-3125 was discovered with ROSAT (Haberl et al. 1997), and its X-ray spectrum was soon found to be well described by a Planckian spectrum with temperature $kT \sim 82$ eV (k being the Boltzmann constant). Similarly to the rest of INS, it is a nearby object (≈ 300 pc, Kaplan et al. 2003) and shows low interstellar absorption ($n_H = 1-1.5 \times 10^{20}$ cm⁻²). More interestingly, it is a confirmed X-ray pulsar with a period of 8.391 s (Haberl et al. 1997) and it is one of the two INSs with a reliable measure of the period derivative $\dot{P} = 7 \times 10^{-14}$ s s⁻¹ (Kaplan & van Kerkwijk 2005a), which implies a magnetic field of about $B = 2.4 \times 10^{13}$ G¹. Another important observational property, common to other INS, is that the observed optical flux is larger (about a factor of 6) than the extrapolation to the optical band of the best blackbody (BB) fit to the X-ray emission. This apparent optical excess flux of

INSs, first observed in RX J1865-3754 can be explained with the existence of large temperature anisotropies over the surface (Pons et al. 2002). In the case of RX J0720.4-3125, the evidence of anisotropic temperature distributions is strongly supported by the observed X-ray pulsations with relatively large amplitude ($\sim 11\%$).

More recently, the story of INSs has suffered a new twist when observations with XMM-Newton have revealed deviations from a pure BB spectrum in the form of absorption features observed in the 0.1 – 1.0 keV band. In the particular case of RX J0720.4-3125, a phase dependent absorption line around 270 eV has been recently reported (Haberl et al. 2004). This feature is normally associated with proton cyclotron resonant absorption and/or bound-bound transitions in H or H-like He (Haberl et al. 2003; van Kerkwijk et al. 2004). Both require a magnetic field of $\sim 5 \times 10^{13}$ G, consistent within with the dipole breaking estimate of 2.4×10^{13} G, but only within a factor 2. Moreover, this estimate only reflects the large scale magnetic field structure, whereas the presence of smaller scale inner magnetic fields (i.e. strong toroidal components) seems very likely because MHD core collapse simulations show that toroidal magnetic fields are quickly generated by differential rotation and early stage convective motions can also create toroidal fields. Strong magnetic fields can affect the emission properties of the

¹ The other object with a measure of the period derivative is RBS 1223, with $\dot{P} = 1.12 \times 10^{-13}$ s s⁻¹, which implies $B = 3.4 \times 10^{13}$ G (Kaplan & van Kerkwijk 2005b)

neutron star surface in multiple ways. For example, they can induce a phase transition turning the gaseous atmosphere into a liquid or solid state (Lai 2001), which results in a spectrum that, besides a reduction in the emissivity compared to a BB, shows some particular features that could explain the observations. This scenario has been extensively studied by different authors (Brinkmann 1980; Turolla et al. 2004; Pérez–Azorín et al. 2005; van Adelsberg et al. 2005). In addition, if the magnetic field is high enough to induce the condensation of the atmosphere, it will also lead to very large anisotropies on the surface temperature distribution (Geppert et al. 2004; Pérez–Azorín et al. 2006; Geppert et al. 2006), providing an attractive scenario to naturally explain the observed large optical excess and pulsed fraction of some isolated neutron stars such as RX J0720.4–3125 and RBS 1223. The case of RX J0720.4–3125 is also particularly interesting because of its clear spectral evolution (de Vries et al. 2004; Haberl et al. 2004; Vink et al. 2004) which has been recently associated with a ~ 7 yr precession period of the neutron star (Haberl et al. 2006).

The paper is organized as follows. In Section 2 we review the main properties of our theoretical model (magnetic field configuration, temperature anisotropy, etc.). In Section 3 we summarize the X–ray observations used in this work and in Section 4 we revisit the phenomenological models previously adopted to describe the data. In section 5, we discuss and motivate the choices made to limit the parameter–space of our models, and we present our main results, obtained by applying our realistic and physically motivated models to the available X–ray data. In Section 6 and 7 we discuss the evidence of precession and the interpretation of the excess optical flux, respectively. Finally, in Section 8, we summarize our results and discuss open questions and caveats.

2. The theoretical model.

In previous papers (Pérez–Azorín et al. 2005; Pérez–Azorín et al. 2006) we have presented the results of detailed calculations of the temperature distribution in the crust and condensed envelopes of neutron stars in the presence of strong magnetic fields, by obtaining axisymmetric, stationary solutions of the heat diffusion equation with anisotropic thermal conductivities. Having explored a variety of magnetic field strengths and configurations, we concluded that variations in the surface temperature of factors 2–10 are easily obtained with $B \approx 10^{13}$ – 10^{14} G whereas the average luminosity (and therefore the inferred effective temperature) depends only weakly on the strength of the magnetic field.

Nevertheless, the luminosity is drastically affected by the field geometry, in particular by the existence of a toroidal component. Moreover, if the magnetic field is strong enough to induce the condensation of the surface, the condensed surface models also predict the existence of a spectral edge that for $B \approx 10^{13}$ – 10^{14} falls in the range 0.2–0.5 keV and that can be consistent with an absorption line such as that reported in RX J 0720.4–3125 (Haberl et al. 2004). We refer to the interested reader to the previous work (Pérez–Azorín et al. 2006) for details about the calculations, and we sketch here only the main

features of the magnetic field geometry and surface temperature distribution.

The structure of relativistic stars with both poloidal and toroidal magnetic field components has recently been studied (Ioka & Sasaki 2004). It was shown that all quantities can be determined from a stream function that satisfies the relativistic Grad-Shafranov equation. In the linear regime (weak magnetic field, in the sense that deformations are small), the Grad-Shafranov equation becomes simpler and, under the assumptions of axisymmetry and stationarity, the general interior solution of the magnetic field has the form (Ioka & Sasaki 2004)

$$\mathbf{B} = B_0 \left(2 \frac{\cos \theta}{r^2} \Psi(r), -\frac{\sin \theta}{r} \frac{\partial \Psi(r)}{\partial r}, \mu \frac{\sin \theta}{r} \Psi(r) \right) \quad (1)$$

where μ is a constant with the interpretation of the wavenumber of the magnetic field. In general, the l -component of the stream function must satisfy the following differential equation

$$\frac{d^2 \Psi(r)}{dr^2} + \left(\mu^2 - \frac{l(l+1)}{r^2} \right) \Psi(r) = 4\pi r^2 \rho a_0, \quad (2)$$

where ρ is the energy density, $a_0 = a_0(r)$ is a function that depends on the boundary conditions and we have omitted the relativistic factors for clarity. In the case $\mu = 0$ the purely poloidal case is recovered, as discussed for example in Konno et al. (1999) for the weak magnetic field limit, and more thoroughly in Bonazzola & Gourgoulhon (1996) for the fully non-linear case. For the general case with both poloidal and toroidal components, a similar non-linear (although Newtonian) analysis is presented in Tomimura & Eriguchi (2005) where Eq. (1) is generalized by considering $\mu = \mu(x)$ as a general function of $x = r \sin \theta A_\phi$, where A_ϕ is the ϕ component of the vector potential.

It is not the purpose of this paper to review all previous calculations about the structure of neutron stars with magnetic fields in detail, but we must stress the more relevant issues that lead us to chose a particular magnetic field structure. The key point is that under the assumptions of stationarity and axisymmetry the electric current (source of the magnetic field) can only have two components, namely a purely toroidal current which produces a poloidal field, and a second term proportional to the magnetic field, and therefore resulting in a force-free field with both poloidal and toroidal components. Thus, the magnetic field is a combination of a force-free component and a purely poloidal one. Since the deformation of neutron stars with the magnetic fields intensity of interest (10^{13} – 10^{14} G) are known to be fairly small, it is reasonable to assume that the field structure can be approximated by the force-free solution (that is $a_0 = 0$ in Eq. (1)). In this case (and in the Newtonian limit) Eq. (2) is a form of the Riccati-Bessel equation, which has analytical solutions (Pérez–Azorín et al. 2006).

In this paper, we will consider force-free solutions with μ chosen to confine the magnetic field to the crust and outer regions, as some of the models discussed in previous works (Geppert et al. 2004; Pérez–Azorín et al. 2006), where it was shown that this crustal confined configurations lead to large anisotropies in the surface temperature distribution. In particular, for our neutron star models, we have considered two cases

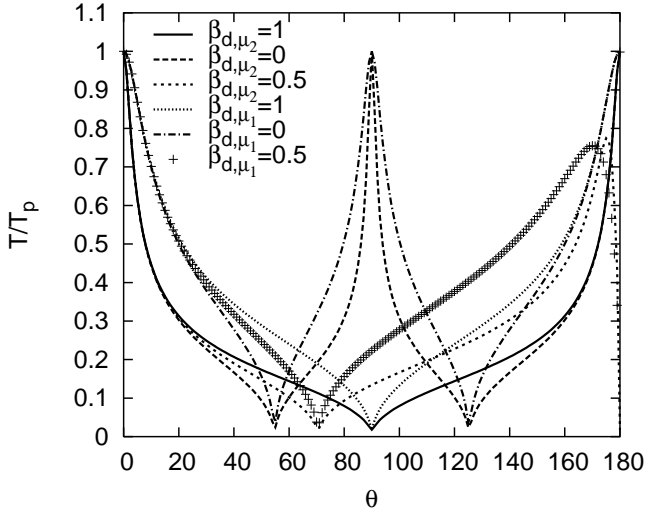


Fig. 1. Surface temperature profiles as a function of the polar angle for different magnetic field configurations according to Eq. 5. We have taken $\mu_1 = 1.34 \text{ km}^{-1}$ and $\mu_2 = 3.877 \text{ km}^{-1}$. The different lines correspond to different relative strengths between the purely dipolar ($\beta_d = 1$) and purely quadrupolar ($\beta_d = 0$) models.

in which $\mu = 1.34 \text{ km}^{-1}$ and $\mu = 3.87 \text{ km}^{-1}$ depending on the considered magnetic field configuration, either purely dipolar or quadrupole-dominated (see Pérez-Azorín et al. (2006) for plots of the magnetic field lines). Notice that μR is roughly the ratio of the toroidal to the poloidal field, while, as mentioned above, μ^{-1} has the interpretation of the typical length scale of the magnetic field.

It turns out that for models in which the toroidal magnetic field covers the whole crustal region (as in force-free configurations) most of the temperature gradient is located in the envelope. Therefore, the classical semi-analytic temperature distribution derived by Greenstein & Hartke (1983)

$$T^4 = T_p^4 \left(\cos^2 \theta_B + \frac{\kappa_{\perp}}{\kappa_{\parallel}} \sin^2 \theta_B \right) \quad (3)$$

remains a good approximation. Here θ_B is the angle between the magnetic field and the normal to the surface. A simple but accurate analytical approximation to the temperature distribution for dipolar force-free models, which is more realistic than discontinuous two temperature models, is

$$T^4(\theta) = T_p^4 \frac{\cos^2 \theta}{\cos^2 \theta + \frac{a+1}{4} \sin^2 \theta} + T_{\min}^4, \quad (4)$$

where T_p is the temperature at the magnetic pole, T_{\min} is the minimum temperature reached in the surface of the star (typically $T_{\min} < 10T_p$) and the parameter a takes into account the relative strength between poloidal and toroidal components. For a dipolar field $a = 0$, while for force-free models with magnetic field confined to the crust and envelope $a \approx 250$. An analogous formula when quadrupolar components are added can also be derived:

$$T^4(\theta) = T_p^4 \frac{f(\theta)^2}{f(\theta)^2 + \frac{a+1}{4} (\beta_d + \beta_q \cos \theta)^2 \sin^2 \theta} + T_{\min}^4,$$

$$f(\theta) = \beta_d \cos \theta + \beta_q (3 \cos^2 \theta - 1) / 2, \quad (5)$$

where β_d and $\beta_q = 1 - \beta_d$ are the relative weights between the dipolar and quadrupolar components. We have found that this approximate expressions are accurate to less than 3%.

It must be mentioned that this force-free structures can be continuously extended into a twisted magnetosphere (Lyutikov et al. 2002; Lyutikov & Gavriil 2006), which has been proposed to be the explanation of the infrared and optical emission of magnetars (Durant & van Kerkwijk 2005). Within this model, the twisted magnetic field is present not only in the magnetosphere, but also in the envelope and probably in the crust of neutron stars.

As an example of temperature distributions, size of the hot spots, and effect of higher order multipoles, in Fig. 1 we show surface temperature profiles as a function of the polar angle for different magnetic field configurations varying from the purely dipolar ($\beta_d = 1$) to purely quadrupolar ($\beta_d = 0$) models. The main features are: i) purely dipolar models show nearly equal antipodal hot polar caps with only minor differences due to the Hall term in the diffusion equation (Geppert et al. 2006; Pérez–Azorín et al. 2006), ii) when a quadrupolar component is present, the north/south asymmetry is broken by the different temperatures and sizes of the polar caps, and iii) a dominant quadrupolar component implies also the existence of a hot equatorial belt, that can be displaced from the equator depending on the relative strength of the dipolar and quadrupolar components. Of course similar but more complex geometries could be obtained by including higher order multipoles. In general, smaller values of μ correspond to larger angular sizes of polar caps and/or equatorial belts.

3. Summary of XMM-Newton observations

RX J 0720.4–3125 has been observed several times by *XMM-Newton* and we focus here on EPIC data (pn and MOS 1) from the 8 publicly available observations. The *XMM-Newton* observations span a period of about 5.5 years starting from May 2000 (Rev. 78) to November 2005 (Rev. 1086). Here we ignore the observations performed with the cameras operated in Small Window because of the worse calibration with respect to Full Frame science modes. The pn data of Rev. 078 are also excluded from the analysis due to problems in the SAS 6.5.0 reduction pipeline (see <http://xmm.vilspa.esa.es/> for details). The remaining data provide a homogeneous set and have all been collected with the cameras operated in Full Frame mode with the Thin or Medium filter applied and a summary of the observations is presented in Table 1. The MOS 2 data are consistent with MOS 1 and do not add relevant information to our analysis. Photon pile-up has been minimised by following standard procedures (see e.g. Haberl et al. 2004). Since the softest energies suffer from calibration uncertainties, we consider the 0.18–1.2 keV band only, after having checked that the inclusion of data down to 0.13 keV does not change our results in any noticeable way (worsening the statistics in a similar way for any spectral model).

In the following we present X-ray data-analysis for all observations by using three different sets of models, a phe-

nomenological one (following previous works by e.g. Haberl et al. 2004; 2006) and two realistic models obtained through detailed numerical simulations in the theoretical framework described above. In all three cases we also consider a sub–set of the pn–FF observations in which we force the absorbing column density to be the same in all observations. For the two realistic models, we also force the model normalization (related to the NS size and distance) and the magnetic field intensity to be the same in all observations.

4. Phenomenological fits revised

As already shown in previous works (de Vries et al. 2004; Haberl et al. 2004; Vink et al. 2004), the X–ray spectral shape of RX J 0720.4–3125 is not that of a pure absorbed black–body (BB). Deviations from a thermal spectrum are seen in the 0.2–0.6 keV band and they are well fitted by models in which a Gaussian absorption line is added to the pure (absorbed) thermal spectrum. The line was interpreted as cyclotron resonance scattering of protons in the NS magnetic field (Haberl et al. 2004). While the above interpretation is certainly allowed by the data, the exact shape of the absorption structure cannot be constrained with high confidence from the X–ray data (Vink et al. 2004) and possibly describes in a phenomenological way the deviations from a pure thermal spectrum. We point out here that BB plus absorption line fits to the X–ray data are phenomenological almost by definition since they cannot account simultaneously for the observed Optical and UV data, underestimating the Optical flux by a large factor. This is the reason why in the following we shall call this description of the X–ray data “phenomenological”.

We repeated this analysis by considering all phase–averaged *XMM–Newton* observations and by describing the spectra with a simple BB plus Gaussian absorption line model, photo–electrically absorbed by a column density of gas, and our results are reported in Table 2. Errors are given at the 90% level for one interesting parameter. The Gaussian absorption line width cannot be constrained with high confidence and it is fixed to its best–fit average value to all observations (75 eV, similar to the 64 eV width imposed by Haberl et al. 2004). We point out that if the Gaussian width is let free to vary, the absorption line energy becomes unconstrained in many cases. All other parameters are free to vary. The final statistics is good for both the pn and MOS 1 cameras and the absorption line is required at more than the 99.99 % confidence level in all observations except Rev. 078, 175, and 622.

As mentioned, we also consider a smaller but more homogeneous sub–set of data from the EPIC–pn camera only, always operated in Full Frame. In this case, since inter–calibration between different instruments is not anymore a concern, we force the absorbing column density to be the same in all observations, as it seems reasonable. Our results are presented in Table 3 and suggest that both the BB temperature and the absorption line equivalent width increase with time. Both quantities increase up to Rev. 815 and decrease in the last observation (Rev. 1086), confirming previous results (Haberl et al. 2006). The temperature variation (from ~ 85 eV to ~ 91 eV) may indicate that the hot spot(s) responsible for the X–ray pulsa-

tions of the source has a different viewing angle (possibly due to precession), yielding to higher and higher effective temperatures (as proposed e.g. in Vink et al. 2004). Evidence for precession in RX J0720.4–3125 has been indeed strengthen in a recent work (Haberl et al. 2006) where a ~ 7 yr periodic variation of the BB temperature has been claimed, based on similar fits (BB and Gaussian absorption line) to the X–ray data. Our results on the variation of the BB temperature are consistent with the inferred period.

5. Spectral analysis with realistic, self-consistent models.

In the previous Section, we discussed simple BB plus absorption line fits to the X–ray spectra of RX J0720.4–3125. We remind here that though such models do provide a very good description of the X–ray data, they cannot explain in a self-consistent way the Optical flux which is observed to exceed by about a factor 6 the predicted one. In the following we present an attempt to describe the X–ray data with synthetic spectra obtained through detailed numerical simulations which can also simultaneously provide a good description of the Optical/UV data.

However, the task of fitting observational data in a multi–parameter space is numerically time–consuming (because it requires computing a large number of models to cover a sufficient number of grid points) and theoretically complex (because it is difficult to avoid falling in local minima in a highly dimensional parameter space). For this reason we have not attempted to solve the problem using brute force but rather to discriminate which parameters are more relevant for each observational fact. We have considered a fiducial NS model fixing the mass at $1.4 M_{\odot}$ and the radius at 12.27 km. While the first choice is well motivated by observations of NSs in binary systems the radius of NSs is much less certain as revealed by our ignorance of the details of the inner nuclear structure and equation of state.

In the present case, however, we are interested in the X–ray (and Optical) emission from the star surface which, in absence of spectral features that can reveal the redshift at the surface, will depend very little on the assumed radius. Indeed, our models are not significantly affected if the NS radius is varied in a sensible range (e.g. 10–15 km). This motivates and justifies the choice of a fiducial model which greatly simplifies the numerical task of computing large grids of models if all parameters are allowed to vary. The magnetic field intensity is defined at the pole and we consider variations in the range of $0.5 - 6 \times 10^{13}$ G, as suggested by the value of 2.4×10^{13} G estimated from the period decay. As for the magnetic field configuration, in the following we will explore two different cases, both confined in the outermost regions (crust and envelope): a purely dipolar magnetic field with $\mu = 1.34 \text{ km}^{-1}$, and a quadrupole–dominated one ($\beta_d = 0.05$) with $\mu = 3.87 \text{ km}^{-1}$. This is only a small sub–set of the possible configurations which has been chosen after a relatively time–consuming assessment of which configuration provides a better description of the X–ray data. In particular, (very) different values for the radial length scale of the magnetic field (μ) resulted in inconsistent results in which the ra-

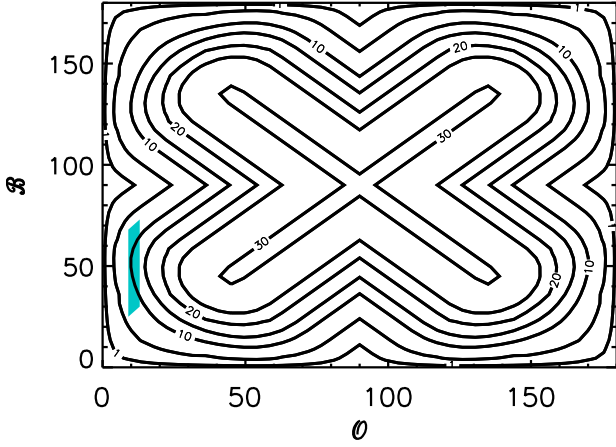


Fig. 2. Contour plots for a purely dipolar magnetic field, with $n_H = 1.33 \times 10^{20} \text{ cm}^{-2}$, $T_p = 115 \text{ eV}$ and $B_p = 1.8 \times 10^{13} \text{ G}$, of the pulsed fraction for a realistic surface temperature distribution. \mathcal{B} is the angle between rotation and magnetic axis, and O the angle between the rotation axis and the observer direction. The flux has been obtained by integration over the whole surface taking into account General Relativistic light bending effects.

dius of the NS, as inferred from the X–ray spectral fits, was different from the fiducial model one.

In the future, we plan to build a much more extensive set of grid models which will be available for X–ray spectral fitting purposes with most of the parameters free to vary. This will result inevitably in a better statistical description of the X–ray data than possible at present. We consider the present work as a first attempt to reproduce the available observational aspects with a realistic self–consistent model, without claiming that the proposed model(s) is (are) the best–possible solution. However, as discussed later, the results inferred from our analysis provide several insights and suggest the direction to take with the goal of improving further the theoretical models and our understanding of INSSs in general.

Having set up a baseline model, we have built tabular XSPEC models² as a function of the pole temperature and magnetic field strength for several orientations within the range allowed by the pulsation profiles, as discussed below. We then consider all the public available *XMM–Newton* observations of RX J 0720.4–3125 and compare our realistic (and limited in parameter–space) models to the data and to the more phenomenological description of the X–ray spectra discussed in the previous Section.

5.1. Purely dipolar magnetic fields.

We begin our analysis with a purely dipolar magnetic field configuration. This is mainly suggested by the observed regular sinusoidal shape of the light curve of RX J0720.4–3125 (when folded at the spin period of 8.391 s). In the framework of our models, the spectral shape and time–evolution mainly depends

on the relative orientation between the magnetic axis, the rotation axis, and the observer line of sight. These can be constrained by using the observed pulsation profile and amplitude of RX J0720.4–3125 as detailed below. In Fig. 2 we show contour plots of the pulsed fraction, for one of our calculations, as a function of the angle between rotation and magnetic axis (\mathcal{B}) and between the rotation and observer direction (O).

First, we can classify the light curves in two groups. The models with large $O + \mathcal{B}$ are characterized by a non sinusoidal pulsation, or even two visible maxima in the pulse profile; this is because we actually can see both poles in each period if $O + \mathcal{B} > 90^\circ$. Therefore, INSSs which exhibit non–sinusoidal pulse profiles do lie in this region. On the other hand, the models with small $O + \mathcal{B}$ always show one single peak in the pulse profile which is very close to sinusoidal when either one of the angles is small. This is probably the case of RX J0720.4–3125, that shows a very regular pulsation profile.

Next, we can reduce the range of angles to those consistent with the observed pulsed fraction. For a nearly spherical neutron star, the rotation axis is essentially aligned with the (vector) total angular momentum of the star, which is conserved. Therefore, the variation of the angle O with time is too small to be observable, but the star wobbles around its symmetry axis (in general different from both, rotation and magnetic axis) with a free precession timescale of a few years for oblateness of the order of 10^{-7} (Jones & Andersson 2001). We have tried different orientations in the range of O and \mathcal{B} allowed by the observed pulsed fraction. We find that the observed pulsed fraction values are best reproduced if $O = 12^\circ$ and \mathcal{B} varies in the range 30° – 60° (i.e. $180^\circ - \mathcal{B}$ in the range 120° – 150°). With this choice of parameters, the pulsed fraction of our models always lies in the range between 9% and 13%, consistent with the observed values. Therefore, we will focus on the vertical shaded region, fixing O and allowing for variations in \mathcal{B} . We have built tabular XSPEC spectral models by fixing $O = 12^\circ$ with the following free parameters: pole temperature KT_{pole} , magnetic field intensity B_p , magnetic field orientation \mathcal{B} , and model normalization R_∞/D_{300} . The model is applied to all available data–sets with the addition of photo–electric absorption.

As for the phenomenological model described above, we first use all the pn and MOS 1 observations with all parameters free to vary. Our results are presented in Table 4. The (unred–shifted) polar temperature varies approximately from 110 eV to 120 eV about 25% larger than the BB temperature of Table 2, while the average effective temperature over the NS surface is about 35–41 eV, more than a factor 2 smaller than the temperature inferred from BB fits. This is due to the very large anisotropy over the surface temperature (a factor 10 between pole and equator) induced by the magnetic field. The X–ray spectrum is dominated by the small hot polar area, while the extended cooler equatorial belt is responsible for most of the optical flux which is well reproduced (see Section 5.5).

The statistical quality of the fits obtained with the realistic models is comparable to that obtained with BB plus Gaussian models (see Table 2 for comparison). However, the accuracy on the most relevant parameters (\mathcal{B} , KT_{pole} , and B_p) is limited by the fact that the inferred variations of n_H drive the fitting results, strongly affecting the soft energy band where most of

² Tabular models are available upon request to the authors

the photons are collected. Given the high proper motion of the source a variation in the absorbing column cannot be excluded, but the observed variation seem to occur almost randomly and the pn and MOS 1 data often give inconsistent results for the same observation. It is much more realistic to assume that the column density is the same in all observations.

To overcome the inter–calibration uncertainties, we consider the pn–FF observations only. As for the BB plus Gaussian fits described above, we force the absorbing column density to be the same in all observations. We also force the model normalization (directly related to the NS radius and distance) and the magnetic field intensity to be the same. Our results are presented in Table 5. As it can be seen by comparing with the results in Table 3, the statistical quality of the fits is worse than in the BB plus Gaussian case. The best–fitting magnetic field intensity B_p is of the order of 1.4×10^{13} G, about a factor 2 smaller than that inferred from the observed period decay, possibly indicating that our model is not an extremely accurate description of the magnetic field geometry.

Despite the above problem, a clear long–term evolution of the magnetic field orientation \mathcal{B} emerges from our results. \mathcal{B} increases with time up to Rev. 815, while it decreases in the last observation (Rev. 1086). By considering the vertical shaded area in Fig. 2 (or its equivalent complementary at $\pi - \mathcal{B}$), this solution suggests that the pulsed fraction must exhibit a long term evolution, with a maximum pulsed fraction around $\mathcal{B} \sim 55^\circ$, corresponding to the latest observations. We point out that the \mathcal{B} long–term evolution has the same behaviour shown by the BB temperature and the absorption line EW (see Table 3), and (see below) pulsed fraction. Our realistic model is thus trying to reproduce the observed variations with a change in the magnetic field orientation, which is what is expected if precession is responsible for the long–term variability.

The model explored so far seems to be able to describe the bulk of the observed long–term variability in terms of precession and is therefore very promising. However, the quality of the fits is not very satisfactory and we thus explore in the following another case in which a strong quadrupolar component is added to the magnetic field configuration.

5.2. Quadrupole–dominated magnetic fields.

In Fig. 3 we show contour plots of the pulsed fraction for one of the models with a dominant quadrupolar component ($\beta_d = 0.05$). The very different surface temperature distribution (two hot spots plus a hot belt close to the equator, as discussed in Section 2) produces significant differences with respect to the purely dipolar case. First, the allowed maximum pulsed fraction is much higher, up to 45%. Second, the north/south symmetry has been broken, and the results are different when changing either \mathcal{B} or O by $\pi - \mathcal{B}$ or $\pi - O$ (the symmetry with respect the simultaneous interchange of both angles by their supplementary is kept). Third, a portion of the hot belt will now be visible, which will have consequences on the spectrum. We proceed as in the previous case, and we first localize the region in which we are allowed to vary the angles O and \mathcal{B} , keeping the pulsed fraction at about 11%, and close to a sinusoidal shape,

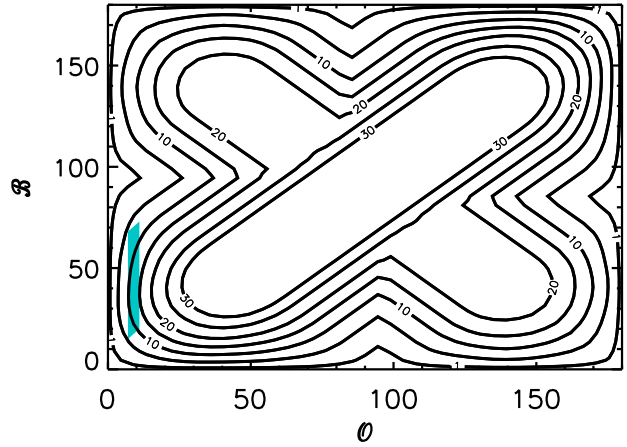


Fig. 3. Contour plots of the pulsed fraction for a realistic surface temperature distribution produced by a quadrupole dominated magnetic field ($\beta_d = 0.05$). The parameters of the model are $T_p = 115$ eV, $B_p = 1.8 \times 10^{13}$ G and $n_H = 1.2 \times 10^{20}$ cm $^{-2}$. The flux has been obtained by integration over the whole surface taking into account General Relativistic light bending effects.

as observed. This corresponds to $O = 11^\circ$ and $\mathcal{B} = 20^\circ - 65^\circ$ (see Fig. 3). As mentioned, $O = 169^\circ$ and $\mathcal{B} = 115^\circ - 160^\circ$ produces the same results.

We proceed as above, first applying the model to all observations and letting all parameters free to vary, and then considering the sub–set of pn–FF data only, forcing the absorbing column density, the model normalization, and the magnetic field intensity to be one and the same in all observations. Our results are presented in Table 6 and Table 7 respectively. When all parameters are free to vary, the statistical quality of the fit is comparable to that obtained with the phenomenological and purely dipolar–field models (Tables 2 and 4) but, as with the purely dipolar model, the variation of the absorbing column density is a possible sign of a degeneracy in the parameters.

We thus regard the pn–FF observations in which the parameters that should remain constant have been forced to be the same in all observations as the most reliable sub–set to infer information on the remaining model parameters (Table 7). In this case, we obtain a very significant improvement with respect to the purely–dipolar model and we approach the statistical quality of the phenomenological fits. With the addition of the quadrupolar component, the best–fitting magnetic field intensity raises to $1.8 \pm 0.2 \times 10^{13}$ G, much closer to the value of $\sim 2.4 \times 10^{13}$ G inferred from the period decay. As for the dipolar model discussed above, the magnetic field orientation \mathcal{B} clearly shows a long–term evolution similar to the $\pi - \mathcal{B}$ evolution of the dipolar model. The issue of the long–term evolution of the magnetic axis orientation will be discussed later in more detail in the framework of the precession interpretation for the variability of RX J0720.4–3125.

5.3. The hardness ratio anti–correlation

The better statistical quality of the fits to the X–ray data and the more consistent value of the magnetic field intensity are, up to some extent, an indication of the presence of higher order multipolar components. However, as recently discussed thoroughly in (Zane & Turolla 2006) there is a more conclusive observational fact that allows us to distinguish between the purely dipolar and the multipolar case. A striking feature of the X–ray light curves of RX J0720.4–3125 is the clear anti–correlation of the hardness ratio with the pulse profiles in both the hard and the soft band. This feature cannot be explained with axisymmetric models that have also a north/south symmetry. A possible explanation that has been proposed is a model with two hot spots with one of them displaced by about 20° from the south pole (Haberl et al. 2006).

Motivated by the well established hardness ratio anti–correlation, we explored whether our models can reproduce the observed behaviour. In Fig. 4 we show the folded light curves in the hard and soft bands, and the hardness ratio for one of the quadrupolar–dominated models used in fitting the X–ray data. The observed anti–correlation of the hardness ratio with the pulse profiles is qualitatively very well reproduced by our model. We point out that such good agreement is impossible to obtain with pure dipolar fields in which the North/South symmetry is not broken. We have not attempted at this stage to find the model that best fits the light curves and the phase averaged spectra at the same time, which is a formidable numerical task, especially when dealing with realistic models that (each one) need computational effort to be produced. However, the good qualitative agreement is indicative that we could be seeing a neutron star with a *hot spot and a hot belt*, as predicted by quadrupole–dominated models, as an alternative to the case of a displaced hot spot.

If the interpretation that all variability is due to free precession of the neutron star is correct, one should be able to find a unique model (temperature, magnetic field configuration, etc.) that explains all observations by only varying the relative orientation and, in our opinion, this model approaches that solution. Our results point in the direction that most of the variation is actually explained by precession of the neutron star. Notice that a precession timescale of a few years has also already been reported for some pulsars (Link & Epstein 2001).

5.4. Precession

As mentioned, evidence for precession in RX J0720.4–3125 has been recently reported by Haberl et al. (2006). The evidence was based on results from BB plus absorption line fits to the available X–ray data in which the BB temperature shows a long–term evolution best described by a sine wave with a period of 7.1 ± 0.5 yr. We consider our results for the dipolar and quadrupole–dominated models (see Table 5 and 7) and try to fit the time evolution of the angle \mathcal{B} which is the relevant quantity as far as precession is concerned. The results are shown in Fig. 5. Notice that the right panel shows $\pi - \mathcal{B}$ for better comparison. This is just a matter of the arbitrary choice of coordinate origin of the polar angle. Both are consistent with the

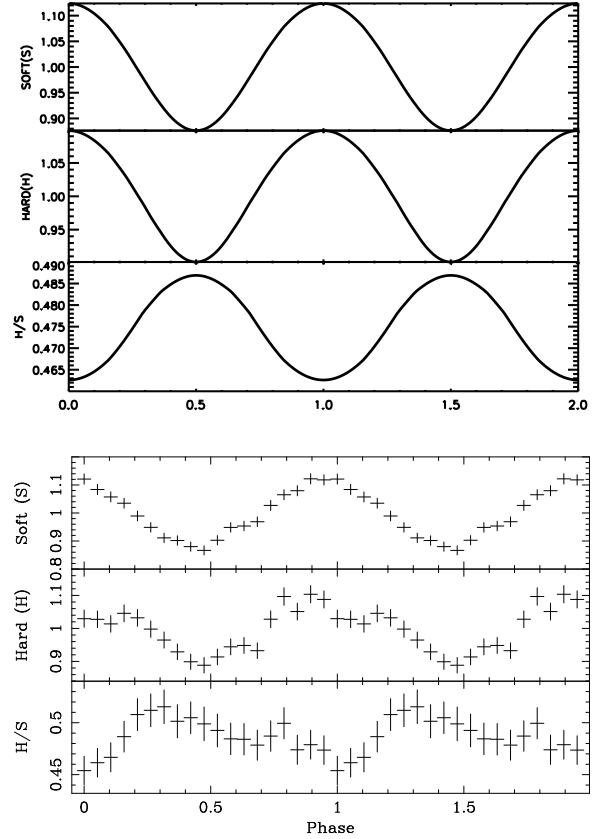


Fig. 4. Pulse profiles in two energy bands (soft:0.12–0.4 keV, hard:0.4–1.0 keV) for a realistic model with $O = 11$, $\mathcal{B} = 54$, $T_p = 115$ eV, $B_p = 1.8 \times 10^{13}$ G, $n_H = 1.2 \times 10^{20}$ cm $^{-2}$ and $\beta_d = 0.05$. The third panel is the hardness ratio (HARD/SOFT). The bottom panel shows the observational data corresponding to observation rev. 534. Notice that we have not attempted to perform a fit of the pulse profiles, it is simply a comparison with the model obtained from spectral fitting. In this figure we have taken into account the response matrix of the instrument and the absorption.

interpretation of a precessing neutron star with a precession period of 7 years and a relatively large wobbling angle of $\approx 20^\circ$. Both the dipolar and quadrupole–dominated cases are very well described by a sine wave but, as mentioned earlier, the hardness ratio anti–correlation strongly favors model with a significant quadrupole component breaking the north/south symmetry. Our results are consistent with the conclusions drawn in (Haberl et al. 2006) with phenomenological models.

5.5. Pulsed fraction long–term evolution

If precession is the right interpretation from the long–term spectral evolution of RX J0720.4–3125, the observed pulsed fraction should also show long timescale variability associated with the variation of the hot spot(s) effective area. We have then extracted 0.12–1.2 keV light curves for the pn observations used above (the Full Frame ones), computed the period of the observed pulsations (always consistent with 8.391 s), and obtained the pulsed fraction for each observation. Our re-

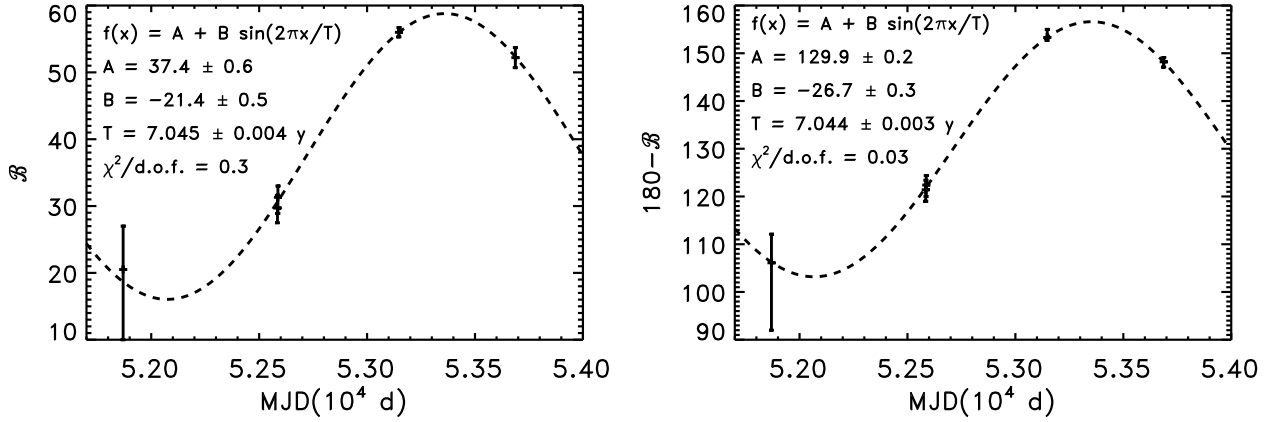


Fig. 5. Time variation of the orientation of the magnetic axis, \mathcal{B} , from the results shown in Tables 5 (left panel, $\beta_d = 1$) and 7 (right panel, $\beta_d = 0.05$). The solid line shows the best fit to the data (see text in figure).

sults suggest that the pulsed fraction is not constant in time, but increased from 10% to 12% on the few years timescale spanned by the observations. We measure a pulsed fraction of $10.1 \pm 0.5\%$ in Rev. 175, $11.1 \pm 0.4\%$ in Rev. 533 and 534, and $11.7 \pm 0.5\%$ in Rev. 815 and $11.9 \pm 0.5\%$ in Rev. 1086. The behaviour is suggestive of a correlation between the BB temperature, the absorption line equivalent width (or deviations from the BB spectrum) and the pulsed fraction, as expected in the precession model.

In Fig. 6 we show the pulsed fraction long-term evolution with the addition of a first data point from Rev 78 (Haberl et al. 2004). The solid line represents a fit with a sine wave in which the period is fixed at 7 yr, while the amplitude is a free parameter. We measure a modulation amplitude of $1.0 \pm 0.3\%$. Although the quality of the data is not high enough to claim a periodic evolution of the pulsed fraction, the obvious consistency with a period of 7 yr (see Fig. 6) strongly supports the precession model. We point out that the pulsed fraction long-term evolution is independent of the adopted spectral model and of the instrument calibrations and represents thereby an independent indication that precession is at work in RX J0720.4–3125.

6. Optical flux

An issue under debate in the condensed surface models is related to the optical flux. When the effect of motion of the ions is neglected the optical flux is very much depressed (Turolla et al. 2004; Pérez–Azorín et al. 2005), but ignoring the motion of ions at low energies is not justified. In fact, a simple treatment of the motion of the ions as free particles leads to very different results (Ginzburg, 1970). This simple approach (to consider them as free particles) could be approximately correct if the surface is in a liquid state, but it is not proper if matter is in solid state and ions are placed in a lattice. However, considering them as totally fixed to the lattice can be as wrong as letting them to move freely. In reality, ions do actually move and resonant plasmon or phonon excitations can be important. Moreover, the strong magnetic fields can modify

the motion of the ions (the ion cyclotron radius is much smaller than the separation between ions in the lattice).

The usual Drude model that describes the microscopic response to electromagnetic fields in metals predicts that the dielectric function ϵ at low energy behaves as

$$\epsilon = 1 - \frac{\omega_p^2}{\omega(\omega + i\Gamma)} \quad (6)$$

where ω_p is the electron plasma frequency ($\omega_p^2 = 4\pi e^2 n_e / m_e$) and Γ is a relaxation coefficient. From this formula it is clear why at very low energy ($\omega \ll \omega_p$) the absorption is strongly suppressed. In the other limit, assuming the motion of the ions is free because they are not bound in a lattice, the effect of the magnetic field is to modify the dielectric function (very schematically, and neglecting damping) as follows

$$\epsilon = 1 - \frac{\omega_p^2}{(\omega + \omega_{B,e})(\omega - \omega_{B,i})} \quad (7)$$

where $\omega_{B,e}$ and $\omega_{B,i}$ are the electron and ion cyclotron frequencies. Therefore, when $\omega < \omega_{B,i}$ the mode which had a large imaginary part of the refraction index is not damped any more (Pérez–Azorín et al. 2006).

But real materials are known to behave in a more complex way than this. The simplest extension of the model that can account for collective excitations of the lattice at characteristic frequencies ($\omega_{0,j}$) is called Drude-Lorentz model, and it consists in the combination of a Drude term with a number of Lorentz oscillators

$$\epsilon = 1 - \frac{\omega_p^2}{\omega(\omega + i\Gamma)} + \sum \frac{\omega_{p,j}^2}{(\omega_{0,j}^2 - \omega^2) - i\omega\Gamma_j} \quad (8)$$

It is clearly out of the scope of this paper to discuss the microphysical behaviour of this condensed (liquid or solid) atmospheres, and we do not know much about the characteristic frequencies of the lattice and how this couples to the magnetic field. We just want to point out that several important energy scales: the ion cyclotron energy $\hbar\omega_{B,i}$, kT , and

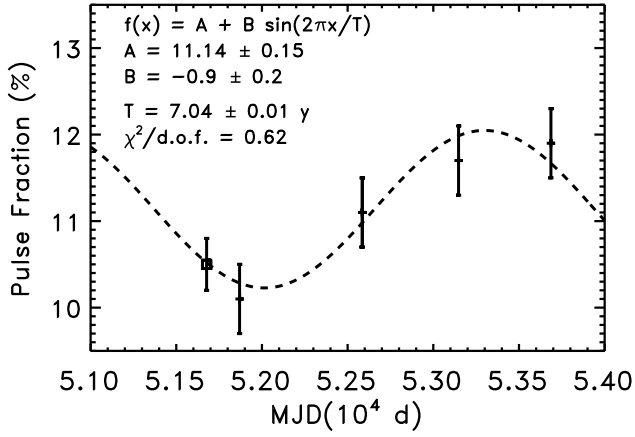


Fig. 6. Variation of the pulsed fraction with time compared with a sinusoidal profile with a periodicity of 7 years.

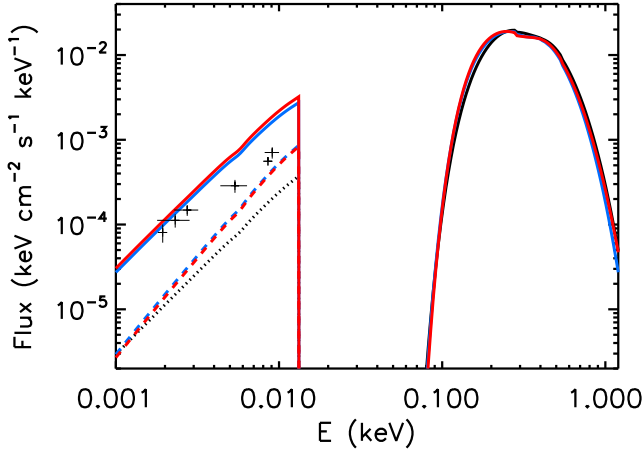


Fig. 7. Spectral energy distribution of the best fits of the revolution 534 for phenomenological model (Table 3, black solid), realistic quadrupolar dominated (Table 7, blue solid), and realistic dipole (Table 5, red solid). The phase-averaged spectra of both models are very similar, and it is necessary to analyze the spectral phase evolution to discriminate. The dotted line is the optical tail of the BB model. Solid and dashed lines in the optical band correspond to models with free and frozen ions, respectively. Available optical and UV data (Kaplan et al. 2003) are also shown (crosses) for comparison.

$\hbar\omega_{p,\text{ion}}$ are similar (about 0.1 keV) under our typical conditions and, consequently, a careful analysis of the emissivity in the optical band is needed before we can establish severe constraints on the models. As a compromise, since the *free ion* treatment predicts an emissivity in the optical band ($\alpha = 1$ corresponds to a blackbody) of about $\alpha = 0.7$ and a *frozen ions* model predicts approximately $\alpha = 0.2$ (Pérez–Azorín et al. 2005; van Adelsberg et al. 2005), we will show both limits in the following figures, so that reality must be placed in between this two different possibilities.

In Fig. 7, we show the unfolded spectra for the best fits to the X-ray spectrum of Rev. 534 together with the available

optical-UV data (Kaplan et al. 2003). We have not attempted to fit simultaneously the optical and X-ray data, but the good agreement is evident. For comparison, we also show (dotted lines) the best BB plus Gaussian fit for the Rev. 534 data to illustrate its similarity with the realistic model in the X-ray band and to highlight the well known problem of under-predicting the optical flux.

Notice that the best fits to the optical observations at lower energies (Jul 2001) show a somewhat higher flux than the latter optical observations (Feb 2002). The fact that the optical observations are not consistent with a pure Rayleigh-Jeans tail has been discussed in detail in (Kaplan et al. 2003) who found that the best fit consists of two BBs plus a power law. However, they also comment that the spectrum can be consistent with a Rayleigh-Jeans tail if the deviations have a temporal nature, which is thought to be unlikely because the X-ray flux is constant. Interestingly, the fact that all observations fall in between the two lines predicted by the *free ions* and *frozen ions* models may be telling us that more effort must be placed in understanding the physics of this emission processes.

7. Summary and conclusions

We have shown that realistic models of neutron stars with strong magnetic fields are consistent with the observed X-ray and optical spectra, the observed deviation from a pure thermal spectrum in the X-ray band, and the long term variability. Although we do not exclude the presence of a resonant proton cyclotron absorption or bound-bound transitions in H, we do not need to invoke it to explain the observed spectral edge. We stress that our model calculates the surface thermal emission, which could further modified by the interaction of the radiation with the plasma in the magnetosphere.

Once the magnetic field configuration is given, we are able to obtain a self-consistently calculated thermal spectrum that reproduces reasonably well all available observations. Our analysis indicates that most of the long-term spectral variation of the source can be explained in terms of neutron star precession. If our interpretation is correct, we predict that the pulsed fraction, effective temperature, and absorption line equivalent width as obtained with phenomenological models, will decrease in subsequent observations of the source, until reaching similar values to Rev. 175. This begins to be apparent in the recent observation Rev. 1086, made public while we were revising the final version of this manuscript. Similar conclusions have been reached independently by other groups (Haberl et al. 2006). Notice, however, that our fits still show some variability of the pole temperature correlated to that of the orientation angle. In theory, if our model were *perfect*, it would give the appropriate surface temperature distribution to explain all variations keeping everything constant except the orientation angle. We have given a step forward in that direction since our fits are obtained keeping fixed n_H , normalization (i.e. distance), and the star model (mass, radius, temperature distribution geometry), but still need to allow for small variations of temperature. Another alternative could be that for some unknown reason (magnetic field evolution, diffusion) the temperature and/or size of the hot regions has changed in a timescale

of 7 years, but we are not aware of any mechanism able to do this in such a short timescale. If this happens to be the case, no periodicity would be expected.

Since we have only explored a few magnetic field configurations an extensive study is very likely to improve the statistical quality of the fits presented here. Nevertheless, we are confident that some qualitative features are quite robust: i) The models that reproduce the observational data have magnetic fields confined to the crust and the outer regions, and strong toroidal components (about an order of magnitude larger than the poloidal one). This naturally leads to large surface temperature variations. ii) Models with strong quadrupolar components are in general favored. Higher order multipoles (octupole, etc) can in principle be added, but a too much patched geometry is in conflict with the large pulsation amplitudes. iii) To explain the anti-correlation of the hardness ratio we need temperature distributions which break the north/south asymmetry. In particular, models with a strong quadrupole predict two hot spots with different temperatures and sizes and a hot belt that can be shifted from the equator.

The emission properties due exclusively to the condensed surface model under consideration are the presence of the spectral edge at about 0.3 keV and the absence of other spectral lines expected from gaseous atmospheres with heavy elements. We think this part of our results is not as robust as the strong anisotropy in the temperature distribution produced by toroidal fields and non dipolar components. There are interesting alternatives that can explain this spectral features equally well, but the physical motivation of the condensed surface is that the magnetic field is high enough to produce the condensation, if the composition is primarily iron or similar heavy elements. Strongly magnetized hydrogen atmospheres (or other light elements) are still an alternative, but to our knowledge there is no fully consistent treatment for arbitrary magnetic field orientations and structure. More work in both lines will be certainly worth to do in the near future.

If future observations confirm that this INS (or others) is subject to precession with a relatively large wobbling angle of $\approx 20^\circ$, combined with a relatively short period of ~ 7 yr, it would have very interesting implications. As pointed out by Link (2003), a large wobbling angle with precession timescale of the order of years is in conflict with the standard picture of a type II superconducting core. This scenario favors either type I superconductivity or a situation in which the magnetic field does not penetrate into the core and it is mainly confined to the crust and outer regions. We point out that this was exactly the starting assumption of our model, a magnetic field living in the crust needed to explain the large surface temperature anisotropies (Pérez–Azorín et al. 2006; Geppert et al. 2006). Alternatively, Jones (2004) suggests that long-term precession leads to the conclusion that nuclei and superfluid neutrons do not coexist, which also would establish severe constraints on the equation of state. At present, the uncertainties in our knowledge of vortex dynamics in the inner crust can lead to different conclusions, all of them interesting and based on the observational confirmation of long-lived under-damped precession.

We also point out that using all available constraints from the X–ray spectra, the pulsed fraction, the pulse profiles and hardness ratios, together with their long–term evolution seems a very promising way of constraining the theoretical models. We plan to use all the available constraints in the near future to relax some of the assumptions made in this work and to explore in much more detail the vast parameter space. We are also working to study other NSs that we expect to be well described by these models. Preliminary results on RBS1223 are promising, since we could find good fits to the very irregular light curve and the large pulsed fraction, again with quadrupolar magnetic fields. Another interesting NS is the pulsar PSR J1119-6127, that has a very high pulsed fraction (70 %). This is impossible to reproduce with purely dipolar components but we found some (still axisymmetric) magnetic field configurations that can explain this extremely large variability. Results about this objects and other isolated neutron stars will be reported in future work in preparation. In parallel, the issue of the magnetic field stability and its diffusion timescale remains open. Our final goal is to find a general solution pointing towards a unified picture in which INSS are just old, cold magnetars whose magnetic fields are a few times smaller than usual, maybe because they have decayed during their lifetime.

Acknowledgements. This work has been supported by the Spanish Ministerio de Ciencia y Tecnología grant AYA 2004-08067-C03-02. JAP is supported by a *Ramón y Cajal* contract from the Spanish MEC.

References

- Brinkmann, W. 1980, A&A 82, 352
- Bonazzola, S. & Gourgoulhon, E., 1996, A&A, 312, 675
- de Vries, C.P., et al., 2004, A&A, 415, L34
- Durant, M. & van Kerkwijk, M.H., 2005, ApJ, 627, 376
- Geppert, U., Küker, M., & Page, D. 2004, A&A, 426, 267
- Geppert, U., Küker, M., & Page, D. 2006, A&A, [arXiv:astro-ph/0512530]
- Ginzburg, V.L., 1970, in Propagation of electromagnetic waves in plasmas (2d ed.; Oxford: Pergamon press)
- Greenstein, G., & Hartke, G. J. 1983, ApJ, 271, 283.
- Haberl, F. Motch, C. Buckley, D. A. H., Zickgraf, F. J., & Pietsch, W. 1997, A&A, 326, 662
- Haberl, F., Schwöpe, A.D., Hambaryan, V., Hasinger, G. 2003, A&A, 403, L19
- Haberl, F., Zavlin, V.E., Trümper, J., Burwitz, V., 2004, A&A, 419, 1077
- Haberl, F. et al. 2006, A&A accepted, [arXiv:astro-ph/0603724]
- Ioka, K. & Sasaki, M., 2004, ApJ, 600, 296
- Jones, D.I. & Andersson, N., 2001, MNRAS, 324, 811
- Jones, P.B. 2004, Phys. Rev. Lett. 92, 149001
- Link, B. 2003, Phys. Rev. Lett. 91, 101101
- Link, B. & Epstein, R.I., 2001, ApJ, 556, 392
- Kaplan, D.L. et al., 2003, ApJ, 590, 1008
- Kaplan, D.L. & van Kerkwijk, M.H., 2005, ApJ, 628, L45
- Kaplan, D.L. & van Kerkwijk, M.H., 2005, ApJ, 635, L65
- Konno, K., Obata, T. & Kojima, Y., 1999, A&A, 352, 211
- Lai, D. 2001, Rev. of Mod. Phys., 73, 629

- Lyutikov, M., Gavriil, F. P., 2006, MNRAS, 368, 690-706
- Lyutikov, M., Thompson, C., Kulkarni, S. R., 2002, ASPC 271, 262
- Pérez-Azorín, J.F., Miralles J.A., & Pons J.A. 2005, A&A, 433, 275
- Pérez-Azorín, J.F., Miralles J.A., & Pons J.A. 2006, A&A, 451, 1009
- Pons, J.A, Walter, F.M., Lattimer, J.M. et al. 2002, ApJ, 564, 981
- Turolla, R., Zane, S., & Drake, J.J. 2004, ApJ, 603, 265
- Tomimura, Y. & Eriguchi, Y. 2005, MNRAS, 359, 1117
- van Adelsberg, M., Lai, D., & Potekhin, A. 2005, ApJ, 628, 902
- van Kerkwijk, M.H., et al. 2004, ApJ, 608, 432
- Vink, J., de Vries, C.P., Méndez, M., & Verbunt, F. 2004, ApJ, 609, L75
- Zane, S. & Turolla, R. 2006, MNRAS, 366, 727

Table 1. XMM-Newton observation information. All observations are performed in Full Frame with the Thin Optical filter applied except in Rev. 175 where the Medium filter was used.

Rev.	Instrument	Epoch	Exposure
78	mos1	2000 May 13	48 ks
175	pn	2000 Nov. 21–22	23 ks
533	pn	2002 Nov. 6–7	26 ks
533	mos1	2002 Nov. 6–7	30 ks
534	pn	2002 Nov. 8–9	27 ks
534	mos1	2002 Nov. 8–9	32 ks
622	mos1	2003 May 2–3	24 ks
711	mos1	2003 Oct. 27–28	14 ks
815	pn	2004 May 22–23	22 ks
815	mos1	2004 May 22–23	26 ks
1086	pn	2005 Nov. 12–13	34 ks

Table 2. The pn and MOS 1 data for all observations are fitted in the 0.18–1.2 keV band with an absorbed BB model including a Gaussian absorption line.

Rev.–Inst.	n_H 10^{20} cm^{-2}	kT (eV)	E_{line} (eV)	$-EW_{\text{line}}$ (eV)	χ^2/dof
078–mos1	$0.72^{+0.35}_{-0.33}$	$84.4^{+1.1}_{-1.8}$	340^{+140}_{-165}	< 20	58/53
175–pn	$0.82^{+0.28}_{-0.42}$	$83.7^{+0.7}_{-1.2}$	249^{+102}_{-105}	< 40	141/152
533–pn	$1.20^{+0.11}_{-0.27}$	$85.0^{+1.1}_{-1.0}$	297^{+22}_{-19}	32^{+11}_{-10}	178/160
533–mos1	$1.20^{+0.25}_{-0.57}$	$87.0^{+1.9}_{-1.8}$	301^{+53}_{-40}	35^{+25}_{-24}	58/50
534–pn	$1.05^{+0.19}_{-0.42}$	$85.7^{+1.1}_{-1.1}$	308^{+18}_{-22}	35^{+8}_{-6}	159/162
534–mos1	$0.82^{+0.31}_{-0.36}$	$86.5^{+1.3}_{-2.5}$	320^{+50}_{-35}	25^{+18}_{-18}	69/51
622–mos1	$1.40^{+0.32}_{-0.82}$	$86.5^{+2.2}_{-1.9}$	350^{+130}_{-150}	< 50	46/48
711–mos1	$1.80^{+1.05}_{-1.10}$	$90.3^{+2.2}_{-2.8}$	370^{+40}_{-55}	45^{+23}_{-21}	47/47
815–pn	$1.32^{+0.35}_{-0.19}$	$91.4^{+1.1}_{-1.2}$	308^{+11}_{-9}	70^{+7}_{-9}	160/163
815–mos1	$1.72^{+0.63}_{-1.05}$	$91.0^{+2.8}_{-2.9}$	370^{+20}_{-20}	50^{+20}_{-15}	50/52
1086–pn	$1.39^{+0.30}_{-0.17}$	$89.6^{+1.2}_{-0.5}$	315^{+9}_{-10}	56^{+6}_{-6}	201/170

Table 3. Joint fits to all EPIC pn and MOS1 for FF mode observations in the 0.18–1.2 keV band with absorbed BB plus absorption Gaussian line model. The absorption is forced to be the same in all observations. NC indicates that a parameter cannot be constrained (i.e. the corresponding model is not required by the data).

Rev.–Inst.	n_H (10^{20} cm^{-2})	KT (eV)	E_{line} (eV)	σ_{line} (eV)	$-EW_{\text{line}}$ (eV)	R_{∞}/D_{300} (km/300 pc)	$\chi^2/d.o.f.$
175–pn	$1.09^{+0.10}_{-0.10}$	$84.45^{+0.05}_{-0.03}$	NC	75^f	NC	$5.5^{+1.2}_{-1.0}$	
533–pn	=	$85.45^{+0.03}_{-0.05}$	289^{+11}_{-10}	=	$33.8^{+3.0}_{-2.8}$	$5.6^{+1.5}_{-1.4}$	
534–pn	=	$85.64^{+0.08}_{-0.04}$	311^{+10}_{-11}	=	$34.4^{+3.1}_{-3.0}$	$5.5^{+1.1}_{-1.3}$	
815–pn	=	$91.61^{+0.05}_{-0.04}$	307^{+5}_{-6}	=	$69.8^{+2.7}_{-2.8}$	$5.0^{+1.2}_{-1.1}$	
1086–pn	=	$90.51^{+0.06}_{-0.03}$	301^{+6}_{-6}	=	$59.3^{+2.4}_{-2.3}$	$5.1^{+1.0}_{-1.2}$	902/811

Table 4. X-ray spectral analysis. Individual fits to the EPIC-pn and EPIC-MOS1 observations in the energy band 0.18-1.2 keV for a purely dipolar magnetic field structure ($\beta_d = 1.0$), $\mu = 1.34$ and $\mathcal{O} = 12^\circ$. We allow to vary the magnetic field intensity at the pole (B_p) and the unredshifted temperature at the pole (kT_{pole}).

Rev.-Inst.	n_H (10^{20}cm^{-2})	\mathcal{B}	kT_{pole} (eV)	R/D_{300} (km/300 pc)	B_p (10^{12} G)	$\chi^2/\text{d.o.f.}$
78-mos1	$0.55^{+0.14}_{-0.20}$	$58.0^{+12.4}_{-8.6}$	$118.1^{+3.7}_{-5.1}$	$14.1^{+10.0}_{-9.3}$	$8.4^{+3.4}_{-3.3}$	54/53
175-pn	$1.06^{+0.11}_{-0.12}$	$52.7^{+18.9}_{-9.2}$	$115.1^{+4.6}_{-2.6}$	$15.2^{+20.4}_{-9.4}$	$10.7^{+2.5}_{-3.8}$	134/152
533-pn	$2.15^{+0.15}_{-0.13}$	$57.4^{+7.1}_{-10.8}$	$111.5^{+3.3}_{-2.6}$	$19.9^{+11.0}_{-11.2}$	$17.4^{+5.4}_{-3.9}$	175/160
533-mos1	$0.79^{+0.96}_{-0.28}$	$26.1^{+35.6}_{-25.1}$	$122.4^{+2.0}_{-3.8}$	$11.3^{+15.2}_{-5.8}$	$24.9^{+10.2}_{-7.1}$	57/50
534-pn	$1.91^{+0.11}_{-0.20}$	$50.6^{+5.6}_{-24.1}$	$113.3^{+5.6}_{-2.2}$	$17.8^{+10.2}_{-10.4}$	$21.5^{+3.1}_{-7.1}$	157/162
534-mos1	$1.00^{+0.35}_{-0.27}$	$63.7^{+4.1}_{-42.2}$	$113.9^{+6.9}_{-6.6}$	$17.4^{+11.7}_{-13.4}$	$14.3^{+24.2}_{-3.7}$	68/51
622-mos1	$2.60^{+0.49}_{-0.32}$	$74.8^{+6.2}_{-10.4}$	$108.3^{+3.3}_{-3.2}$	$25.3^{+7.3}_{-7.8}$	$15.0^{+21.8}_{-10.0}$	45/48
711-mos1	$2.39^{+0.65}_{-0.31}$	$54.2^{+8.5}_{-8.5}$	$123.6^{+2.2}_{-1.2}$	$15.1^{+11.5}_{-7.2}$	$25.0^{+9.4}_{-5.6}$	50/47
815-pn	$2.53^{+0.09}_{-0.09}$	$44.1^{+2.3}_{-1.8}$	$124.8^{+1.0}_{-0.5}$	$13.9^{+5.5}_{-5.5}$	$25.0^{+0.9}_{-0.5}$	193/163
815-mos1	$2.40^{+0.32}_{-0.25}$	$55.1^{+3.5}_{-5.0}$	$123.8^{+2.0}_{-1.1}$	$14.9^{+7.3}_{-10.1}$	$25.0^{+3.0}_{-2.1}$	55/52
1086-pn	$2.68^{+0.06}_{-0.07}$	$49.2^{+1.3}_{-1.5}$	$121.9^{+0.4}_{-0.3}$	$16.1^{+4.3}_{-6.0}$	$25.0^{+0.5}_{-0.5}$	232/170

Table 5. Joint fits to EPIC FF mode observations for a purely dipolar field ($\beta_d = 1$) with $\mu = 1.34$ and $\mathcal{O} = 12^\circ$, forcing the hydrogen column density, the normalization constant and the magnetic field intensity to be the same for all observations.

Rev.-Inst.	n_H (10^{20}cm^{-2})	\mathcal{B}	kT_{pole} (eV)	R/D_{300} (km/300 pc)	B_p (10^{12} G)	$\chi^2/\text{d.o.f.}$
175-pn	$1.33^{+0.04}_{-0.02}$	$20.5^{+6.5}_{-10.5}$	$120.6^{+0.2}_{-0.6}$	$11.3^{+1.1}_{-1.8}$	$14.1^{+0.6}_{-0.2}$	
533-pn	=	$29.7^{+1.9}_{-2.2}$	$123.3^{+0.3}_{-0.4}$	=	=	
534-pn	=	$31.3^{+1.7}_{-2.4}$	$123.5^{+0.4}_{-0.4}$	=	=	
815-pn	=	$56.0^{+0.7}_{-0.7}$	$132.3^{+0.5}_{-0.4}$	=	=	
1086-pn	=	$52.2^{+1.5}_{-1.5}$	$131.2^{+0.3}_{-0.7}$	=	=	1570/819

Table 6. Individual fits to the EPIC-pn and EPIC-MOS1 observations in the energy band 0.18-1.2 keV for a quadrupole dominated magnetic field ($\beta_d = 0.05$) with $\mu = 3.87$ and $\mathcal{O} = 11^\circ$. We allow to vary the magnetic field intensity and the temperature at the pole.

Rev.-Inst.	n_H (10^{20}cm^{-2})	\mathcal{B}	kT_{pole} (eV)	R/D_{300} (km/300 pc)	B_p (10^{12} G)	$\chi^2/\text{d.o.f.}$
78-mos1	$0.43^{+0.37}_{-0.27}$	$56.0^{+88.0}_{-27.1}$	$105.6^{+2.1}_{-1.1}$	$12.5^{+9.4}_{-6.0}$	$14.2^{+21.9}_{-9.2}$	56/53
175-pn	$0.89^{+0.13}_{-0.14}$	$70.7^{+65.0}_{-18.0}$	$104.4^{+0.5}_{-0.5}$	$13.3^{+9.7}_{-4.9}$	$39.6^{+11.6}_{-11.7}$	138/152
533-pn	$1.71^{+0.08}_{-0.10}$	$51.2^{+3.4}_{-6.7}$	$104.2^{+0.5}_{-0.17}$	$16.2^{+6.1}_{-5.7}$	$54.4^{+6.6}_{-8.4}$	173/160
533-mos1	$0.83^{+0.79}_{-0.31}$	$31.4^{+36.4}_{-13.3}$	$106.4^{+1.3}_{-2.0}$	$15.2^{+9.9}_{-8.5}$	$24.9^{+20.0}_{-11.9}$	57/50
534-pn	$1.65^{+0.07}_{-0.14}$	$47.4^{+2.6}_{-7.0}$	$104.1^{+0.6}_{-0.3}$	$16.4^{+6.0}_{-5.9}$	$55.0^{+5.0}_{-10.4}$	160/162
534-mos1	$0.41^{+0.27}_{-0.40}$	$43.5^{+9.6}_{-26.1}$	$104.9^{+1.6}_{-1.2}$	$14.4^{+10.0}_{-7.7}$	$43.7^{+11.3}_{-18.3}$	69/51
622-mos1	$0.44^{+0.64}_{-0.39}$	$59.3^{+108.0}_{-49.6}$	$106.6^{+1.6}_{-1.3}$	$11.8^{+12.5}_{-5.7}$	$24.9^{+22.7}_{-19.8}$	45/48
711-mos1	$2.56^{+0.39}_{-0.88}$	$32.7^{+6.14}_{-8.2}$	$107.7^{+7.5}_{-1.4}$	$17.2^{+11.1}_{-11.9}$	$55.0^{+5.0}_{-25.0}$	50/47
815-pn	$1.99^{+0.09}_{-0.11}$	$25.6^{+1.7}_{-1.6}$	$111.9^{+1.8}_{-0.6}$	$15.4^{+3.0}_{-3.1}$	$25.0^{+1.2}_{-0.9}$	206/163
815-mos1	$2.00^{+0.27}_{-0.40}$	$36.7^{+3.2}_{-6.2}$	$109.9^{+2.5}_{-0.8}$	$15.4^{+9.1}_{-7.5}$	$54.0^{+6.0}_{-8.4}$	54/52
1086-pn	$1.90^{+0.03}_{-0.07}$	$25.4^{+1.2}_{-1.0}$	$109.5^{+0.5}_{-1.3}$	$16.5^{+3.2}_{-3.0}$	$25.0^{+0.9}_{-0.7}$	255/170

Table 7. Joint fits to EPIC-pn and EPIC-MOS1 FF mode observations for a quadrupole dominated magnetic field ($\beta_d = 0.05$) with $\mu = 3.87$ and $O = 11^\circ$, forcing the hydrogen column density, the normalization constant and the magnetic field intensity to be the same for all observations.

Rev.–Inst.	n_H (10^{20} cm^{-2})	\mathcal{B}	kT_{pole} (eV)	R/D_{300} (km/300 pc)	B_p (10^{12} G)	$\chi^2/\text{d.o.f.}$
175	$1.23^{+0.04}_{-0.04}$	$73.9^{+6.0}_{-14.1}$	$104.6^{+0.4}_{-0.4}$	$12.7^{+1.0}_{-2.1}$	$18.2^{+1.6}_{-1.5}$	
533	=	$58.6^{+2.0}_{-2.4}$	$107.5^{+0.2}_{-0.3}$	=	=	
534	=	$57.6^{+2.0}_{-2.4}$	$107.5^{+0.4}_{-0.3}$	=	=	
815	=	$26.9^{+1.7}_{-0.6}$	$118.2^{+0.5}_{-0.2}$	=	=	
1086	=	$31.8^{+0.9}_{-1.1}$	$116.3^{+0.5}_{-0.3}$	=	=	1192/819